

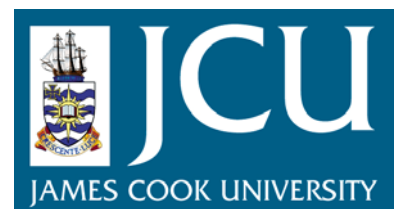
JCU ePrints

This file is part of the following reference:

Mao, Yadan (2009) *Unsteady natural convection in near-shore waters*. PhD thesis, James Cook University.

Access to this file is available from:

<http://eprints.jcu.edu.au/10962>



Unsteady Natural Convection in Near-Shore Waters

**Thesis submitted by
Yadan Mao, B.Sc., M.Sc.
in December 2009**

**for the degree of Doctor of Philosophy
in the School of Engineering & Physical Sciences
James Cook University**

Statement of access

I, the undersigned, author of this work, understand that James Cook University will make this thesis available for use within the University Library and, via the Australian Digital Theses network, for use elsewhere.

I understand that, as an unpublished work, a thesis has significant protection under the Copyright Act and;

I do not wish to place any further restriction on access to this work.

25/03/2010

Yadan Mao

Date

STATEMENT ON SOURCES

Declaration

I declare that this thesis is my own work and has not been submitted in any form for another degree or diploma at any university or other institution of tertiary education. Information derived from the published or unpublished work of others has been acknowledged in the text and a list of references is given.

.....
(Signature)

.....
(Date)

Electronic copy

I, the undersigned, the author of this work, declare that the electronic copy of this thesis provided to the James Cook University Library is an accurate copy of the print thesis submitted, within the limits of the technology available.

Yadan Mao

25/03/2010

Date

Acknowledgements

First and foremost, I would like to express my deep gratitude to my supervisors A/Prof. Chengwang Lei and Prof. John C. Patterson for their guidance, support and encouragement throughout my PhD study. The many valuable discussions we had during our weekly meetings enlightened me on my study. Their academic conscientiousness sets an example for my future research.

I would also like to thank our group members Dr. Feng Xu and Dr. Suvash Saha. Their help in getting me familiar with the software FLUENT is greatly appreciated.

It is also a pleasure to thank Prof. Malcolm Heron, who was my previous supervisor when I was studying for PhD in the area of Physical Oceanography. Although due to unexpected events, he retired and could not continue to be my supervisor, his encouragement and help enabled me to publish my nine months' work with him in the *Journal of Physical Oceanography*. After he retired, I transferred to the School of Engineering and started over as a PhD student for the current project.

My sincere thanks to Prof. Helene Marsh, the Dean of the Graduate Research School, for her continual support and encouragement throughout my journey of PhD study, especially during my transfer to the School of Engineering.

Many thanks also go to all the staff in the School of Engineering and Physical Sciences, James Cook University for creating a thoroughly enjoyable place to do research. Advice from Dr. Wenxian Lin and A/Prof. Zhongxiao Peng for presentation skills and career planning is gratefully appreciated. I am also grateful for the friendly atmosphere provided by my office mate Mr. David Henderson.

The PhD scholarship jointly awarded by China Scholarship Council and James Cook University is gratefully acknowledged.

Last but not least, my deep thanks to my parents for their unconditional love, understanding and support. Although far away from them during my study as an international student here, their spiritual support and encouragement have been always accompanying me and guiding me.

Abstract

In the near-shore waters of natural water bodies, an increasing depth in the offshore direction is a geometric factor which results in differential heating or cooling across the shore. Exposed to daylight radiation, the volumetric heating rate in the shallow region is greater than in the deep region, generating a warm surface layer flowing offshore. At night, a circulation in the opposite direction is induced by differential cooling owing to heat loss from the water to the atmosphere. Field experiments demonstrate that this natural convection in calm near-shore waters plays a significant role in cross-shore exchanges with significant biological and environmental implications. This thesis aims to provide detailed quantification of this thermal flow for various thermal forcing conditions.

Based on a wedge model, an improved scaling analysis is proposed in the present study to reveal more detailed features of the flow than the previous scaling analysis, especially the dependency of flow properties on offshore distance. Four different types of thermal forcing (radiative heating, isoflux cooling, constant and ramped isothermal heating) are considered in the scaling analysis, and the scaling results are verified by the corresponding numerical simulations.

For heating induced by absorption of radiation, two critical functions of the Rayleigh number with respect to offshore distance are derived from scaling analysis to identify the distinctness and stability of the thermal boundary layer at any local position. These two functions reveal four possible flow scenarios, depending on the bottom slope and the maximum water depth. For each flow scenario, the flow domain may be composed of multiple subregions with distinct thermal and flow features, depending on the Rayleigh number. The dividing positions between neighboring subregions and the flow properties in each subregion are quantified by scaling. The scenario of relatively large bottom slope and shallow water is examined in detail and classified into three flow regimes based on the Rayleigh number. For the unstable flow regime, the entire flow domain is composed of three subregions, with the dominant mode of heat transfer changing from conduction to stable convection and finally to unstable convection as offshore distance increases. Characteristics of instability are investigated through a comprehensive spectral analysis which reveals the dependency of spectral properties on water depth, offshore distance and the Rayleigh number.

For isoflux cooling on the water surface, flow scenarios revealed by scaling analysis share similarity with that of the radiation heating, although the mechanisms of these two cases are significantly different. The distinctness and stability of the thermal boundary layer are identified by two critical Rayleigh number functions, a comparison between which reveals two possible flow scenarios depending on the bottom slope. The scenario with relatively large bottom slopes is examined in detail and further classified into three possible flow regimes depending on the Rayleigh number.

For constant and ramped (increasing linearly with time) isothermal heating at the water surface, a hybrid of approximate analytical solutions and scaling analysis is used to quantify the flow in the conductive region and scaling analysis is developed for the convective region. For the conductive region, the problem is simplified into a one dimensional conduction problem with a variable local water depth. The analytical solutions of the simplified problem agree well with the numerical results obtained by solving the full Navier-Stokes equations. It is revealed that for the conductive region, when the thermal boundary layer reaches the local bottom at time t_{sp} , the local velocity reaches a maximum value for constant heating, and for ramp heating, the flow becomes steady at time t_{sp} if the ramp duration is larger than t_{sp} . For both constant and ramped heating, flow in the conductive region eventually becomes isothermal and stationary. The dependency of the maximum velocity and steady state velocity on various flow parameters is quantified by scaling. For the convective region, a comparison between the ramp duration P and the time it takes for convection to balance conduction reveals two scenarios: if the ramp finishes before the balance, no steady state is reached within the ramp duration, and after the ramp finishes, the flow velocity continues to increase and gradually becomes steady, whereas if the ramp finishes after the balance, a quasi-steady state is reached within the ramp duration, and the flow becomes steady soon after the ramp finishes. For both scenarios, the flow reaches the same steady state velocity as the corresponding constant heating case.

Table of Contents

Statement of access	i
Statement of sources declaration	ii
Electronic copy	iii
Acknowledgements	iv
Abstract	v
List of figures	xi
List of tables	xx
Nomenclature	xxi
Chapter 1 Introduction	1
1.1 Problem description	1
1.2 Literature review	4
1.2.1 Constant radiation heating	7
1.2.2 Constant surface cooling	11
1.2.3 Time varying thermal forcing	14
1.2.4 Summaries	15
1.3 Thesis aims and outline	16
Chapter 2 Unsteady near-shore natural convection induced by absorption of radiation	19
2.1 Introduction	19
2.2 Model formulation	20
2.3 Scaling analysis	22
2.3.1 Initial stage of boundary layer development	22
2.3.2 Steady state of the boundary layer	24

2.3.3	Instability of thermal boundary layer.....	27
2.4	Discussion of possible flow regimes.....	28
2.5	Numerical procedures	33
2.5.1	Governing equations	33
2.5.2	Numerical method.....	34
2.6	Numerical verification of the scaling analysis	37
2.6.1	Flow scenarios and distinctive regions in different flow regimes	37
2.6.2	Initial stage scaling	45
2.6.3	Steady state scaling for distinct regions.....	47
2.6.4	Critical time for the onset of instability	52
2.7	Conclusions.....	53
Chapter 3 Characteristics of instability of radiation-induced natural convection in shallow littoral waters		57
3.1	Introduction.....	57
3.2	Mesh and time-step dependency tests.....	62
3.3	Development of instability.....	64
3.3.1	Development of spatial features	64
3.3.2	Time series at different x and Ra.....	68
3.4	Identification of the quasi-steady state	70
3.5	Spectral variation	71
3.5.1	Spectral variation with water depth and Ra	72
3.5.2	Spectral variation with offshore distance and Ra.....	74
3.5.3	Power of instability over the entire domain	80
3.6	Conclusions.....	81
Chapter 4 Unsteady near-shore natural convection induced by surface cooling		85
4.1	Introduction.....	85

4.2	Model formulation	87
4.3	Scaling analysis.....	88
	4.3.1 Initiation of the flow.....	88
	4.3.2 Steady state of the boundary layer	89
	4.3.3 Onset of instability	91
	4.3.4 Possible flow regimes	93
4.4	Numerical procedures	95
	4.4.1 Governing equations	95
	4.4.2 Numerical method.....	96
4.5	Verification of scaling analysis.....	97
	4.5.1 Flow scenarios in different flow regimes.....	99
	4.5.2 Steady-state scaling for distinct regions.....	104
4.6	Conclusions.....	107
Chapter 5 Unsteady natural convection in a reservoir induced by isothermal heating at the water surface.....		111
5.1	Introduction.....	111
5.2	Model formulation	113
5.3	Numerical procedures	115
	5.3.1 Governing equation.....	115
	5.3.2 Numerical methods and tests	115
5.4	Theoretical analysis and numerical simulations for constant heating	117
	5.4.1 Analytical solution and scaling for the conductive region.....	117
	5.4.2 Scaling analysis and simulations for the convective region.....	126
5.5	Theoretical analysis and simulations for ramp isothermal heating.....	130
	5.5.1 Analytical solution and scaling for conductive region.....	131
	5.5.2 Scaling analysis and simulations for convective region	141
5.6	Conclusions.....	146

Chapter 6	Conclusions and further work	149
6.1	Conclusions.....	149
6.1.1	Natural convection induced by absorption of radiation	149
6.1.2	Natural convection induced by iso-flux surface cooling.....	151
6.1.3	Natural convection induced by constant and ramped isothermal heating.....	151
6.2	Further work.....	153
References	157
Appendix A	Numerical Method	163
A.1	Formulation.....	163
A.2	Numerical schemes	165
A.3	Convergences	168

List of figures

Figure 1.1 Wedge model characterizing the cross-shore geometry with the x axis representing the offshore direction.	6
Figure 1.2 Distinct subregions with characteristic isotherms in the unstable flow regime for radiation heating: Region I, conductive; Region II, stable convective; Region III unstable. (Mao <i>et al.</i> 2009a).	10
Figure 1.3 Distinct subregions with characteristic isotherms in the unstable flow regime for surface cooling: Region I, conductive; Region II, stable convective; Region III, unstable. (Mao <i>et al.</i> 2009c).	13
Figure 2.1 Geometry of the flow domain.	21
Figure 2.2 Typical profiles of $f_1(x)$ and $f_2(x)$ for (a) $A > Ra_c^{-1/2}, h < 4/\eta$; (b) $A > Ra_c^{-1/2}, h > 4/\eta$; (c) $A < Ra_c^{-1/2}, h < 4/\eta$; and (d) $A < Ra_c^{-1/2}, h > 4/\eta$. Horizontal dotted lines represent typical flow regimes. The Rayleigh numbers of the filled squares separate the different Rayleigh number regimes.	29
Figure 2.3 Sketches of expected isotherms in different flow sub-regions: Region I, $Ra < f_1(x)$, indistinct, conductive; Region II, $f_1(x) < Ra < f_2(x)$, distinct, stable convective; Region III, $Ra > f_2(x)$, unstable convective.....	30
Figure 2.4 A typical profile of $f_1(x)$ and $f_2(x)$ for scenario (a) plotted with parameter values used in numerical simulations; horizontal lines represent the actual Ra values used in the numerical simulations.....	35
Figure 2.5 Time histories of the maximum negative horizontal component of velocity in the bottom boundary layer obtained along the vertical line at $x = 3.33$ for $Ra = 1.4 \times 10^7$ with two different meshes. (a) with a linear time scale (b) with a logarithmic time scale.	36
Figure 2.6 Features of the thermal flow at a low Ra ($Ra < A^{-2}e^{\eta h}$) at the steady state. (a) Isotherms with an interval of 2.11, (b) streamlines with an interval of 0.0525 of clockwise flow and (c) profile of the horizontal heat transfer rate averaged over the local water depth for $Ra = 70$	38

Figure 2.7 Features of thermal flow in the medium Ra regime ($A^{-2}e^{\eta h} < Ra < Ra_c^3 A^4 e^{\eta h}$) at the steady state. (a) Isotherms with an interval of 1.6887 for $Ra = 3500$, (b) Isotherms with an interval of 0.8444 for $Ra = 35000$, and profiles of the horizontal heat transfer rate at (c) $Ra = 3500$ and (d) $Ra = 35000$39

Figure 2.8 Dividing position between conduction-dominated and convection-dominated regions from the numerical simulation versus that from scaling analysis. The dashed line represents the predicted minimum value of the dividing position under a stable condition from scaling analysis.40

Figure 2.9 Features of thermal flow in the high Ra regime ($Ra > Ra_c^3 A^4 e^{\eta h}$) at the quasi-steady state (a) Isotherms with an interval of 0.063 at $Ra = 1.4 \times 10^6$, (b) Isotherms with an interval of 0.042 at $Ra = 1.4 \times 10^7$. The lower plots in (a) and (b) are zoomed views of the left hand section of the cavity indicated by the two vertical dashed lines. (c) Streamlines with an interval of 7 at $Ra = 1.4 \times 10^6$. (d) Streamlines with an interval of 14 at $Ra = 1.4 \times 10^7$. Dashed streamlines represent clockwise flow, and solid streamlines represent anticlockwise flow. (e) and (f) are the profiles of the horizontal heat transfer rates averaged over local water depth for $Ra = 1.4 \times 10^6$ and $Ra = 1.4 \times 10^7$ respectively.41

Figure 2.10 (a) Standard deviation of convection time series over a time period of 0.04 at the quasi-steady state (b) Dividing position between the stable and unstable regions from numerical simulations versus the prediction from scaling.43

Figure 2.11 Time series of the horizontal heat transfer rates averaged over the local water depth at $Ra = 1.4 \times 10^6$ for three representative x positions (a) $x = 0.5$ (b) $x = 1.5$ (c) $x = 4$44

Figure 2.12 Verification of initial temperature scaling with respect to time at $x=5.0$. (a) Temperature profiles normal to the bottom surface at different times (b) Normalized temperature profiles.45

Figure 2.13 Verification of initial temperature scaling with respect to the horizontal position x at time $t = 8.0 \times 10^{-4}$, (a) Non-dimensional temperature profiles normal to the bottom surface at different non-dimensional x . (b) Normalized temperature profiles at different horizontal positions.46

Figure 2.14 Volumetric flow rate at different x positions within the conduction-dominated near shore region for different Rayleigh numbers. The x positions are equally spaced within the specified range.48

Figure 2.15 Volumetric flow rate at different x positions within the conduction-dominated near shore region for different Rayleigh numbers. The x positions are equally spaced within the specified range.	48
Figure 2.16 Maximum velocity extracted along vertical lines at various x positions within the stable convection region. The x positions are equally spaced within the specified range. (a) and (c) are maximum negative horizontal component of velocity in the bottom boundary layer. (b) and (d) are maximum horizontal component of velocity in the upper layer.	49
Figure 2.17 Volumetric flow rate at different x positions within the stable convection region under different Rayleigh numbers. The x positions are equally spaced within the specified range.	50
Figure 2.18 Contours of the mean flow at quasi-steady state for $Ra = 1.4 \times 10^6$ (a) Streamlines at an interval of 3.5 (b) Isotherms at an interval of 0.042.....	51
Figure 2.19 Maximum horizontal velocity extracted along vertical lines at different horizontal positions within the convection dominated region (extending to the unstable convection region for the last four Rayleigh numbers for which instability occurs) (a) Maximum negative horizontal velocity u in the bottom layer (b) Maximum horizontal velocity u in the upper layer. The horizontal positions are extracted at equal intervals within the specified range.	51
Figure 2.20 Critical time of instability at different horizontal positions from the numerical simulation of Lei & Patterson (2003) versus the present scaling prediction.	52
Figure 3.1 Stability diagram of an inclined layer in a rectangular box filled with water, $Pr = 7$, aspect ratio = 10:4:1. Experimental results (from Kirchartz & Oertel 1988).....	58
Figure 3.2 Spectra of the time series of the vertical velocity v at $x = 4.0$, $y = -0.3$ for $Ra = 1.4 \times 10^7$ from different meshes.	64
Figure 3.3 Isotherms (a), (b) and streamlines (c), (d) at the initial stage for $Ra = 1.4 \times 10^6$ at different times. Dashed streamlines represent clockwise flow.	65
Figure 3.4 Isotherms (a)-(d) and streamlines (e)-(h) at the transitional stage for $Ra = 1.4 \times 10^6$ at different times. Dashed streamlines represent clockwise flow while solid streamlines represent anti-clockwise flow.	66

Figure 3.5 (a) Isotherms and (b) Streamlines for $Ra = 1.4 \times 10^6$, dashed lines represent clockwise flow.	68
Figure 3.6 Time series of flow properties at different horizontal positions for $Ra = 1.4 \times 10^6$. (a) horizontal convection rate $conv(x)$ integrated over the local water depth; (b) temperature at different x values along the line of $y = -0.1x + 0.33$, which is close to and parallel to the sloping bottom.....	69
Figure 3.7 Time series of horizontal component of velocity at $x = 2.67$, $y = -0.23$ for different Rayleigh numbers.....	70
Figure 3.8 Time series of horizontal component of velocity at the position of (4.33, -0.4) and spectra of different sections of the time series for $Ra = 2.1 \times 10^6$. (a) Time series with a logarithmic time scale. (b) Time series with a linear time scale. (c) Time series of 0.1~0.2. (d) Time series of 0.2~0.3. (e) Time series of 0.35~0.45 (quasi-steady state). (f) Spectra before quasi-steady state. (g) Spectra during the quasi-steady state. .	71
Figure 3.9 Spectra of vertical velocity at various depths. (a) Spectra at various depths along the line of $x = 3.33$ for $Ra = 2.1 \times 10^6$. (b) Normalized spectra along $x = 3.33$ for $Ra = 2.1 \times 10^6$. (c) Spectra at various depths along the line of $x = 4.17$ for $Ra = 3.5 \times 10^6$. (d) Normalized spectra along $x = 4.17$ for $Ra = 3.5 \times 10^6$	72
Figure 3.10 Standard deviation of the time series of the vertical velocity during the quasi-steady state at various water depths: (a) $x=3.33$ for $Ra = 2.1 \times 10^6$. (b) $x=4.17$ for $Ra = 3.5 \times 10^6$	73
Figure 3.11 Time series of the average horizontal convection $conv(x)$ over the local depth for $Ra = 2.1 \times 10^6$ (a) $x = 3.33$ (b) $x = 4.17$. The lower plots of (a) and (b) are the zoomed views of the time series at the quasi-steady state.	74
Figure 3.12 The spectra of time series of horizontal convection $conv(x)$ at the quasi-steady state at $x = 3.33$ (left) and $x = 4.17$ (right) for different Rayleigh numbers. (a) $Ra = 1.4 \times 10^6$ (b) $Ra = 2.1 \times 10^6$ (c) $Ra = 3.5 \times 10^6$	75
Figure 3.13 Spectra of the average horizontal convection $conv(x)$ normalized by the maximum power of each x position for different Rayleigh numbers. (a) $Ra = 1.4 \times 10^6$ (b) $Ra = 2.1 \times 10^6$ (c) $Ra = 3.5 \times 10^6$ (d) $Ra = 1.4 \times 10^7$	76
Figure 3.14 Spectra of the average volumetric flow rate $Q(x)$ normalized by the maximum power of each x position for different Rayleigh numbers. (a) $Ra = 1.4 \times 10^6$ (b) $Ra = 1.4 \times 10^7$	77

Figure 3.15 Spectra of velocity component parallel to the slope along $y = -0.1x + 0.033$ normalized by the maximum power of each x position for different Rayleigh numbers. (a) $Ra = 1.4 \times 10^6$ (b) $Ra = 2.1 \times 10^6$ (c) $Ra = 3.5 \times 10^6$ (d) $Ra = 1.4 \times 10^7$ 78

Figure 3.16 Standard deviation of velocity component parallel to the bottom slope along $y = -0.1x + 0.33$ for different Rayleigh numbers. (a) Linear scale (b) Logarithmic scale. 79

Figure 3.17 Dividing positions between stable and unstable region predicted from scaling versus those from numerical simulations. 80

Figure 3.18 Standard deviation of vertical velocity over the entire domain (a) $Ra = 1.4 \times 10^6$, (b) $Ra = 1.4 \times 10^7$ 80

Figure 4.1 Profiles of $f_1(x)$ and $f_2(x)$ for (a) $A > Ra_c^{-1/2}$ (b) $A < Ra_c^{-1/2}$. Horizontal dotted lines represent typical flow regimes. 94

Figure 4.2 Sketches of expected isotherms for different flow subregions: (I) $Ra < f_1(x)$ indistinct, conductive; (II) $f_1(x) < Ra < f_2(x)$, distinct, stable convective; (III) $Ra > f_2(x)$, unstable convective. 94

Figure 4.3 Time histories of the maximum negative horizontal component of velocity in the surface boundary layer along the vertical line of $x = 3.5$ for $Ra = 3.5 \times 10^7$ 97

Figure 4.4 Typical profiles of $f_1(x)$ and $f_2(x)$ for scenario (a) plotted with parameter values used in the numerical simulations; horizontal lines represent Ra values used in the numerical simulations. 98

Figure 4.5 Flow properties in the conductive regime of $Ra < A^{-2}$, $Ra = 70$ (a) Isotherms at an interval of 1.90. (b) Anticlockwise streamlines at an interval of 0.035. (c) Horizontal heat transfer rate averaged over the local water depth. The curve of the total heat transfer rate overlaps with the curve of the conduction heat transfer rate. 100

Figure 4.6 Flow properties in the conductive regime of $A^{-2} < Ra < Ra_c^3 A^4$. (a) Isotherms for $Ra = 2.1 \times 10^3$ with an interval of 1.4073. (b) Isotherms for $Ra = 2.1 \times 10^4$ with an interval of 0.7036. Horizontal heat transfer rate averaged over the local water depth for (c) $Ra = 2.1 \times 10^3$ and (d) $Ra = 2.1 \times 10^4$ 100

Figure 4.7 Dividing position between conduction- and convection-dominated regions from the numerical simulations versus that from scaling analysis. The dashed line

approximately indicates the dividing position corresponding to the critical Rayleigh number for the switch from stable to unstable flow regime from the scaling analysis. 101

Figure 4.8 Flow properties at the quasi-steady state in the unstable convective regime of $Ra > Ra_c^3$. (a) Isotherms at an interval of 0.0422 for $Ra = 3.5 \times 10^6$. (b) Isotherms at an interval of 0.0169 for $Ra = 3.5 \times 10^7$. The interval of the isotherms in the enlarged region of both (a) and (b) is 0.0422. (c) Streamlines at an interval of 7 for $Ra = 3.5 \times 10^6$. (d) Streamlines at an interval of 14 for $Ra = 3.5 \times 10^7$. Solid streamlines represent anti-clockwise flow and dashed lines represent clockwise flow. (e) Horizontal heat transfer rate for $Ra = 3.5 \times 10^6$. (f) Horizontal heat transfer rate for $Ra = 3.5 \times 10^7$ 102

Figure 4.9 (a) Standard deviation of time series of horizontal convection over a time period of 0.12 for different Rayleigh numbers. (b) Dividing positions between the stable and the unstable subregions from numerical simulations versus those from scaling analysis. 103

Figure 4.10 Time series of the maximum negative horizontal velocity at $x = 3.5$ for two different Rayleigh numbers. 103

Figure 4.11 Volumetric flow rates and the maximum velocities extracted from simulation versus their respective scaling for the conduction-dominated region. (a) Volumetric flow rates. (b) Maximum negative horizontal velocity in the surface layer. (c) Maximum horizontal velocity in the bottom layer. 105

Figure 4.12 Volumetric flow rates and the maximum velocities extracted from simulations versus their respective scaling for the stable-convection-dominated region. (a) Volumetric flow rates. (b) Maximum negative horizontal velocity in the surface layer. (c) Maximum horizontal velocity in the bottom layer. 106

Figure 4.13 Contours of the time-averaged flow over a period of 0.12 during the quasi-steady state for $Ra = 2.1 \times 10^6$. (a) Streamlines at an interval of 10, dashed lines represent clockwise flow and solid lines represent anticlockwise flow. (b) Isotherms at an interval of 0.07. 107

Figure 4.14 The maximum velocities extracted along vertical lines at different horizontal positions within the unstable region ($x = 0.27 \sim 0.36$ at an equal interval for all the Rayleigh numbers) for the time-averaged mean flow. (a) The maximum negative horizontal velocity in the surface layer (b) The maximum horizontal velocity in the bottom layer. 107

Figure 5.1 Sketch of the flow domain and the coordinate system. 113

Figure 5.2 Time series of the maximum horizontal velocity along the vertical line of $x = 3.5$ for $Ra = 2 \times 10^7$ for different grids.	116
Figure 5.3 Vertical temperature profile obtained from analytical solution (black line) and numerical solution (red line) for $A = 0.05$. ‘Nu’ = numerical, ‘An’ = analytical. .	118
Figure 5.4 Time series of temperature averaged over the local water depth obtained from numerical simulations (‘Nu’) and analytical solutions (‘An’). (a) $A = 0.05$ (b) $A = 0.1$	120
Figure 5.5 Normalized temperature gradient at various offshore distances obtained from the numerical simulation (‘Nu’), the analytical solution (‘An’), and the approximate analytical solution (‘Ap’). (a) $A = 0.05$. (b) $A = 0.1$	121
Figure 5.6 Normalized temperature gradient at various offshore distances and bottom slopes (a) results from numerical simulations (b) numerical results normalized by scaling predictions.	122
Figure 5.7 Verification of the maximum velocity in the time series and its corresponding time (a) Time series of the maximum horizontal velocity extracted along vertical lines from numerical simulations at different x , A and Ra (b) Time series of the maximum horizontal velocity normalized by the scaling results.	125
Figure 5.8 (a) The maximum velocity in the time series from numerical simulation versus scaling prediction (b) The time corresponding to the maximum velocity from simulation results versus scaling prediction.	126
Figure 5.9 Profile of $f(x)$	127
Figure 5.10 Verification of distinct boundary layer (a) Temperature contours for $Ra = 3 \times 10^6$ (b) Temperature contours for $Ra = 2 \times 10^7$ (c) Temperature profiles along the vertical line of $x = 8.3$ (d) Thickness from simulation versus that from scaling analysis.	129
Figure 5.11 (a) Time series of the maximum velocity along the vertical line at different offshore distances for $Ra = 10^6$. (b) Time series of the maximum velocity normalized by the steady state scaling.	130
Figure 5.12 Time series of temperature at different positions from numerical simulations (Nu) and analytical solutions (An) (a) $P = 0.04$ for $P < t_{sp}$ (b) $P = 0.4$ for $P > t_{sp}$. Analytical solution applies for $t \leq P$	133

Figure 5.13 Verification of the steady state time and steady state temperature for the long ramp period of $P = 0.4$. (a) Time series of temperature at different positions for different bottom slopes. (b) Time series normalized by the steady state scales. 134

Figure 5.14 Time series of the temperature averaged over the local water depth at different offshore distances from numerical simulations (Nu) and analytical solutions (An) (a) $P = 0.04$ for $P < t_{sp}$ (b) $P = 0.4$ for $P > t_{sp}$. The analytical solutions apply for $t \leq P$ 135

Figure 5.15 Time series of the temperature averaged over the local water depth at different offshore distances from numerical simulations (Nu) and analytical solutions (An) (a) $P = 0.04$ for $P < t_{sp}$ (b) $P = 0.4$ for $P > t_{sp}$ 135

Figure 5.16 Time series of the horizontal temperature gradient at different offshore distances from numerical simulations (Nu), analytical solutions (An) and the approximate solution (Ap) for two different scenarios. (a) $P = 0.04$ for $P < t_{sp}$ (b) $P = 0.4$ for $P > t_{sp}$ 137

Figure 5.17 Verification of the steady state scales of the horizontal temperature gradient for the long ramp period of $P = 0.4$. (a) Time series of average temperature at different offshore distances for different bottom slopes. (b) Time series normalized by the steady state scales..... 137

Figure 5.18 Verification of the steady scales for time and flow velocity for the long ramp case of $P > t_{sp}$ (a) Time series of the maximum flow velocity along the vertical lines at different parametric settings for $P = 0.04$ (b) Time series of the maximum flow at different parametric settings for $P = 0.4$ (c) Time series in (a) and (b) normalized by the respective steady state scale for time and velocity. 139

Figure 5.19 The steady state velocity within the ramp duration from numerical simulations versus scaling predictions..... 139

Figure 5.20 Verification of the maximum velocity and the corresponding time for the short ramp case, $A = 0.05$, $P = 0.04$. (a) Time series of the maximum flow velocity at different offshore distances for different Ra . (b) Time series normalized by the scales of the maximum velocity and the corresponding time respectively..... 140

Figure 5.21 The time series of horizontal velocity along the line of $x = 3.5$ for the two different scenarios (a) $P = 0.04 < t_{sp}$, $Ra = 10^6$ (b) $P = 0.4 > t_{sp}$, $Ra = 2 \times 10^7$ 144

Figure 5.22 Time series of horizontal velocity at $x = 4.67$ for the short ramp duration scenario, $P = 0.04 < t_{sp}$ (a) numerical results for different Rayleigh numbers (b) numerical results normalized by velocity scale at P	144
Figure 5.23 Time series of the maximum velocity along the vertical line of $x = 3.5$ for the long ramp scenario of $P > t_{sp}$ (a) numerical results for different Ra and P (b) numerical results normalized by the quasi-steady scales of (5.67) and (5.68).	145
Figure A.1 Typical mesh used in this thesis	165
Figure A.2 Flow chart of the pressure-based solver	166
Figure A.3 One-dimensional control volume	167

List of tables

Table 2.1 Rayleigh numbers adopted in the numerical simulations for radiation heating	34
Table 3.1 Properties of the vertical velocity v at $x = 4.0$, $y = -0.3$ for different grids	63
Table 4.1 Various Rayleigh numbers adopted in the numerical validation.....	98
Table 5.1 The maximum horizontal velocity u at $x = 3.5$ and $x = 4.5$ for different grids	117
Table A.1 Convergence criteria for different thermal forcing.....	169

Nomenclature

A	bottom slope
\vec{A}	surface area vector enclosing the control volume in (A.13)
a, b	coefficient of the discretized equation (A.19)
$Conv(x)$	convection integrated over the local depth at offshore distance x
$\overline{Conv(x)}$	convection averaged over the local depth at offshore distance x
C_p	specific heat
f	the lowest frequency of harmonic mode
f_d	the most dominant frequency
$f_1(x)$	critical function of Rayleigh number for distinct thermal boundary layer
$f_2(x)$	critical function of Rayleigh number for unstable thermal boundary layer
F_y	buoyancy force in the y momentum equation
g	acceleration due to gravity
h	the maximum water depth
$H(x)$	horizontal heat transfer rate averaged over the local depth at offshore distance x
H_0	volumetric heating intensity at the water surface ($= I_0 / \rho C_p$)
I_0	radiation intensity at the water surface
k	thermal conductivity
m	coefficient of the QUICK scheme (A.14)
\hat{n}	coordinate normal to the sloping bottom
p	pressure
P	the duration of the ramp heating
P_d	power of the most dominant frequency
Pr	Prandtl number
$Q(x)$	Flow rate integrated over the local depth at offshore distance x
$\overline{Q(x)}$	Flow rate averaged over the local depth at offshore distance x
Ra	global Rayleigh number
Ra_c	critical Rayleigh number of instability
$Ra_c(0^\circ)$	critical Rayleigh number of instability for horizontal fluid layers
Ra_L	local Rayleigh number of the thermal boundary layer

S	Internal heating source
S_ϕ	source of ϕ per unit volume in the general transport equation (A.13)
std	standard deviation of the time series at quasi-steady state
t	time
t_B	time for the onset of instability
t_c	time for the thermal boundary layer to reach steady state
t_d	time for the thermal boundary layer to diffuse over the local water depth
t_m	time for the local flow to reach the maximum velocity and the maximum horizontal temperature gradient
t_{sp}	steady state time within the ramp duration
T	temperature
T_a	temperature increase through absorption of radiation
T_b	temperature increase through bottom heat flux in the radiation heating case
T_S	temperature decrease through surface heat flux in the cooling case
T_0	initial temperature
T_1	Difference between the local temperature and the average temperature
\bar{T}	the average temperature over the local water depth
u	component of velocity in the x direction
u_{max}	the maximum horizontal component of velocity
u_p	velocity at the time that ramp finishes for the short ramp scenario
u_{sp}	steady state velocity within the ramp duration
u_s	velocity at quasi-steady state for the long ramp scenario
v	component of velocity in the y direction
\vec{v}	velocity vector
V	control volume
x	coordinate in the horizontal direction
x_0	dividing position between distinct and indistinct thermal boundary layer
x_1	dividing position between stable and unstable subregions
x_2	dividing position between unstable middle region and stable offshore region for the deep water case in radiation heating
y	coordinate in the vertical direction

Greek symbols

α	under-relaxation factor
β	thermal expansion coefficient
ΔT	temperature difference between the water surface and the initial temperature for constant isothermal heating
Δt	time step
$\Delta\phi$	variation of ϕ at each iteration
δ_T	thickness of the thermal boundary layer
δ_d	thickness of the distinct thermal boundary layer at steady state for constant isothermal heating
ϕ	quantity to be solved in the general transport equation
ϕ_{old}	value of ϕ in the previous iteration
Γ_ϕ	diffusion coefficient for ϕ in the general transport equation
η	bulk attenuation coefficient for water
κ	thermal diffusivity
μ	dynamic viscosity
ν	kinematic viscosity
ρ	density
ρ_0	initial density
θ	inclination angle of the thermal layer
τ	Normalized temperature difference between the local position and the water surface
$\bar{\tau}$	Normalized average temperature over the local depth
$\bar{\tau}_s$	Normalized steady state average temperature over the local depth
$\left. \frac{\partial \bar{\tau}}{\partial x} \right _s$	Temperature gradient at steady state within the ramp duration

Subscript

f	face of the control volume
i, j	tensor indices
p	cell P
nb	neighbouring cells of cell P

Superscript

n Time level of iteration